Aerospace Science and Technology 24 (2013) 264–274

Contents lists available at SciVerse ScienceDirect

Aerospace Science and Technology

www.elsevier.com/locate/aescte

Thermochemical exploration of hydrogen combustion in generic scramjet combustor

Malsur Dharavath, P. Manna, Debasis Chakraborty *

Computational Combustion Dynamics Division, Directorate of Computational Dynamics, Defence Research & Development Laboratory, P.O. – Kanchanbagh, Hyderabad, India

ARTICLE INFO

Article history:
Received 16 December 2010
Received in revised form 16 November 2011
Accepted 24 November 2011
Available online 2 December 2011

Keywords:
Scramjet
Reacting flow
Turbulence–chemistry interaction

ABSTRACT

Numerical exploration of non-reacting and reacting flow field of hydrogen fueled scramjet combustor is presented. Three-dimensional Navier–Stokes equations with K–ε turbulence model are solved using a commercial CFD solver. A combination of Eddy Dissipation (ED) and Finite Rate Chemistry (FRC) models is used to model combustion. The complex shock and expansion wave structures and their interactions are well captured in the simulation. The computed wall pressures match very well with the experimental values. Computed velocity profiles match nicely with the experimental results in the near wake region but overpredict the values in the far field region. It has been observed that the periodic boundary condition predicts early onset of reaction but the reaction zone is much boarder and intense for the full combustor simulation. Full combustor simulations predict the temperature profile more accurately and maximum deviation is of the order of 12%. Detailed H_2–air chemistry is required to get better match of temperature field in the near wake regions.

1. Introduction

The development of the efficient propulsion systems capable of producing large thrust is the key for the success of the hypersonic vehicle development programs. The combustion must take place at supersonic speed when the flight Mach number is above 6.0 to maintain permissible temperature and pressure at the combustion chamber with reasonable combustion efficiency. Scramjet propulsion system with hydrogen fuel is one of most promising candidates for providing thrust for these vehicles. The flow field inside a scramjet combustor is highly complex. The mixing of reactants, flame holding, and stability and completion of combustion are the major concerns in supersonic speed in the combustion chamber.

Heiser and Pratt [8] provided an overview of the preliminary concept of fuel–air mixing and mixing controlled supersonic combustion. Considerable efforts have been focused on different injection schemes like cavity, strut, pylon for different geometrical configurations and flow conditions in the past two decades. Selected methods that have been used to enhance the mixing process in the scramjet engines are summarized and reported in Ref. [17]. The problem of slow lateral fuel transport in the air stream can be circumvented by injecting the fuel in the core region of the flow by means of struts and or pylons. The oblique shocks generated from the struts also augment the mixing which is very much needed in high speed propulsion devices. Reduction of losses and increase in momentum are very important for efficient design of scramjet combustor. Parallel injection of hydrogen fuel has often been contemplated in high speed operating envelope of scramjet combustor to reduce the injection losses and to take advantage of incremental momentum of the fuel stream. A good number of experimental and numerical studies [6,7,12–14,18,19] were reported in the literature to focus on various aspects of flow phenomena including drag losses, mixing, combustion, intake combustor interaction, etc., in strut based scramjet combustors with hydrogen fuel. These studies mostly measure and compare the wall properties (surface pressure and heat flux) and exit profiles for various flow parameters. Detailed diagnostics of flow distribution, namely, temperature and species mass fraction across a cross section inside the combustor is very limited. Scramjet experiments with hydrogen fuel in a simple geometry at the Institute for Chemical Propulsion of German Aerospace Center at DLR [20–22] provide important wall pressure distribution as well as velocity and temperature profiles at different cross sections in the combustor. In these experiments, hydrogen was injected from the base of a wedge-shaped strut at sonic speed parallel to an airstream of $M = 2.0$. Measured wall pressures and velocity and temperature profiles across the cross section can act as an important data base for CFD model validation in scramjet combustor flow. RANS [15,23] and LES [2,5] calculations for this experimental condition are presented in the literature to address the effect of combustion model, unstructured grid on the flow development. Wepler et al. [23] presented RANS calculations with K–ε turbulence model and Probabilistic Euler Lagrangian (PEuL) based combustion model while Oevermann [15] used a two equation K–ε turbulence model

* Corresponding author. Tel.: +91 40 24583323; fax: +91 40 24340037.
E-mail address: debasis_cfd@drdl.drdo.in (D. Chakraborty).

1270-9638/$ – see front matter
doi:10.1016/j.ast.2011.11.014

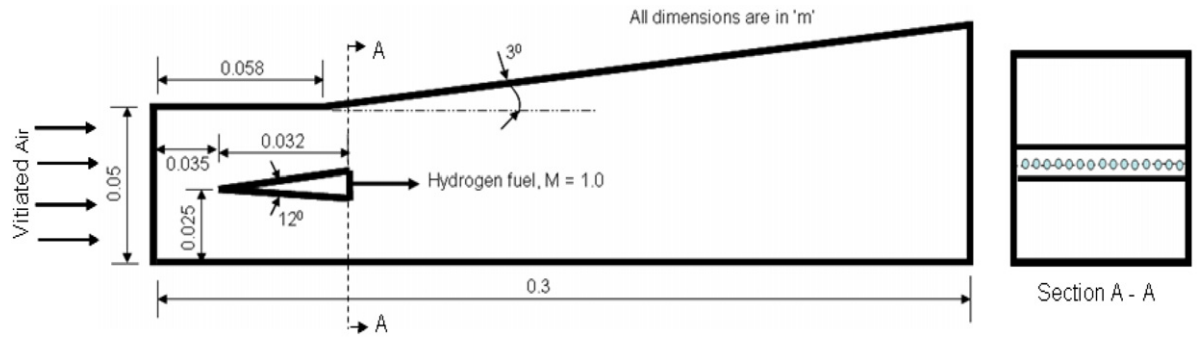

Fig. 1. Schematic sketch of the DLR scramjet combustion chamber.

combined with stretched laminar flamelet model for turbulent diffusion flame. Coupling between turbulence and non-equilibrium chemistry was achieved via a statistical description of the mixture fraction with a presumed β-Probability Density Function (PDF). Although LES study of Berglund and Fureby [2] showed a reasonable match with the experimental values, it reported some discrepancies concerning the volumetric expansion and time averaged velocities. Genin et al. [5] use Large Eddy Simulation and Linear Eddy Model (LES-LEM) approach to simulate the Oevermann experimental condition. Although, the use of LES-LEM model has improved the temperature profile prediction compared to RANS based model, there is significant difference between the prediction and experimental results. It is clear that modeling issues in high speed turbulent reactive flows need further investigation. The higher order turbulence and combustion models are computationally prohibitive for practical engineering applications.

In this work, the experimental investigations of Waidmann et al. [20–22] have been explored numerically with K–ε turbulence model, simple chemical kinetic scheme and simple turbulence–chemistry interaction model to find the capability of these standard engineering tools to predict the mixing and combustion characteristics in a scramjet combustor. Three-dimensional Navier–Stokes equations are solved using commercial CFD software. Computed thermochemical behaviors of the flow field are compared with experimental results.

2. Experimental conditions and computational details

Experimental conditions of Waidmann et al. [20–22] have been discussed adequately in the literature. In the experiment, preheated air (heated by combustion of hydrogen with air in a heater) is expanded through a Laval nozzle and enters in the combustion inlet at $M_a = 2.0$. The combustor has a constant area section of 0.058 m from the combustor inlet. This is followed by a divergence section (one sided divergent combustor) of 0.242 m length with 3° divergent angle at upper wall, provided to compensate for the expansion of the boundary layer. The width and the length of the combustor are 0.045 m and 0.3 m respectively. The heights of the combustor at inlet and outlet are 0.05 m and 0.068 m respectively. A wedge-shaped strut is placed at the middle in the combustion chamber at 0.035 m downstream from the combustor inlet. The length and half-wedge angle of the strut are 0.032 m and 6° respectively. Hydrogen fuel is injected parallel to the air stream (vitiated air) through 15 numbers of holes with a diameter of 0.001 m placed 0.0028 m apart (along the width) at the middle of the strut base. Fig. 1 shows the schematic of the combustor geometry with the physical dimensions. The flow conditions of the incoming air stream and the hydrogen fuel are taken from Ref. [20] and are given in Table 1. Combustion was initiated by pre-burning of a small amount of O_2 in a H_2 tube by a spark.

Since the injection holes are equal in size and placed in equidistance along the width, the flow behavior of the holes and adjacent region is almost symmetrical (except the two side wall-adjacent holes). Hence, one injection hole along with both side adjacent regions (up to middle of the two adjacent injection holes) has been considered for the computational domain. The computational domain and typical grid structure are shown in Fig. 2.

Table 1
Inflow conditions of the air stream and the hydrogen jet.

Parameters	Air	Hydrogen
Mach number	2.0	1.0
Axial velocity (m/s)	730	1200
Static temperature (K)	340	250
Static pressure (bar)	1	1
Density (kg/m^3)	1.002	0.097
O_2 mass fraction	0.232	0
H_2O mass fraction	0.032	0
N_2 mass fraction	0.736	0
H_2 mass fraction	0.0	1

In the simulation, X-axis is taken along the length, Y-axis along the height and Z-axis along the width with the origin being placed at middle of the bottom wall. Structured grid with the typical size $540 \times 75 \times 30$ is generated for the computational domain using ICEM-CFD [1]. The grids are clustered towards the upper, lower, and strut wall as well as in the wake region of the strut to capture high gradient flows in these regions. In the present study four different types of boundary conditions are applied. Supersonic inflow has been imposed at the inlet of the combustor and H_2 injection hole and supersonic outflow has been considered at the outlet of the combustor. Adiabatic wall condition is imposed on top and bottom wall of combustor and strut surface. Symmetry condition is imposed on two sides of the domain.

3. Computational methodology

CFX-11 [1] is an integrated software system capable of solving diverse and complex multi-dimensional fluid flow problems. The software solves 3D Reynolds Averaged Navier–Stokes (RANS) equations in a fully implicit manner. It is a finite volume method and is based on a finite element approach to represent the geometry. The method retains much of the geometric flexibility of finite element methods as well as the important conservation properties of the finite volume method. It utilizes numerical upwind schemes to ensure global convergence of mass, momentum, energy and species. In the present study, the discretization of the convective terms is done by the first-order upwind difference scheme. Local time stepping has been used to obtain steady-state solutions. The turbulence model used was K–ε model with wall functions. The combustion is modeled using combination of infinitely fast rate kinetics based on Eddy Dissipation (ED) and Finite Rate Chemistry (FRC) models. The details of the governing equations, thermodynamics, combustion models and the discretization schemes are given in the following subsections. To find out the accuracy and the range

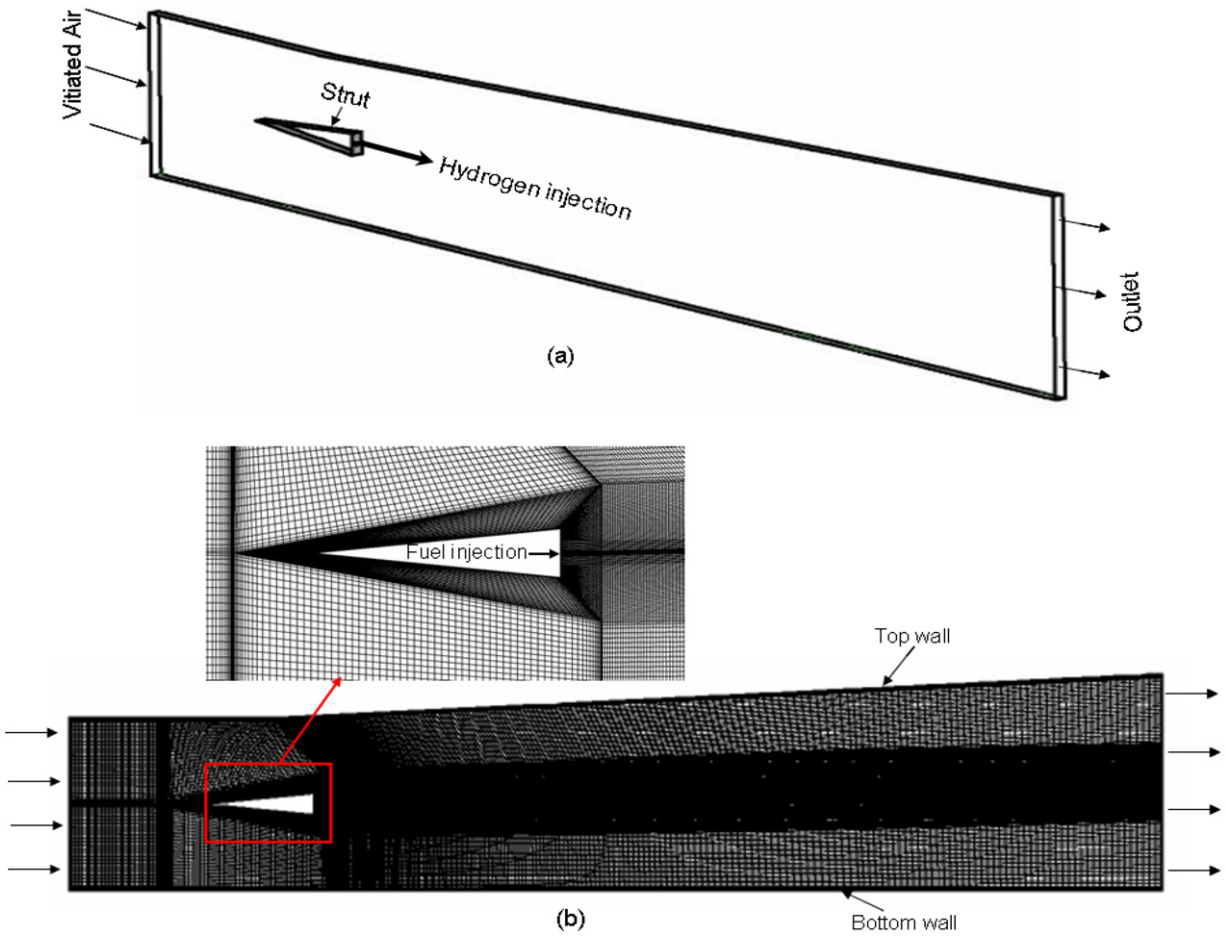

Fig. 2. (a) Computational domain, and (b) grid distribution on combustor with zoomed at strut region.

of applications, the software has been validated for various reacting and non-reacting flows pertaining to the scramjet combustor including transverse sonic injection in supersonic flow [10], transverse H_2 injection in constant area duct [11], staged H_2 injection from struts [16] and pylon injectors [9]. All these validation exercises have revealed that although, the computed pressures overpredict the experimental values in the injection zone, the computational and experimental values of the flow parameters match fairly well in the divergent portion of the combustor where the major portion of thrust is produced.

3.1. Governing equations

The appropriate system of equations governs the turbulent flow of a compressible gas may be written as

Continuity equation:

$$\frac{\partial \rho}{\partial t} + \frac{\partial}{\partial x_k}(\rho u_k) = 0, \quad k = 1, 2, 3$$

Momentum equation:

$$\frac{\partial}{\partial t}(\rho u_i) + \frac{\partial}{\partial x_k}(\rho u_i u_k) + \frac{\partial P}{\partial x_i} = \frac{\partial(\tau_{ik})}{\partial x_k}, \quad i, k = 1, 2, 3$$

Energy equation:

$$\frac{\partial}{\partial t}(\rho H) + \frac{\partial}{\partial x_k}(\rho u_k H) = -\frac{\partial}{\partial x_k}(u_j \tau_{jk}) + \frac{\partial q_k}{\partial x_k}, \quad j, k = 1, 2, 3$$

Turbulent kinetic energy (K) equation:

$$\frac{\partial}{\partial t}(\rho K) + \frac{\partial}{\partial x_k}(\rho u_k K) = \frac{\partial}{\partial x_k}\left(\left(\frac{\mu_l}{\mathrm{Pr}} + \frac{\mu_t}{\sigma_K}\right)\frac{\partial K}{\partial x_k}\right) + S_K$$

Rate of dissipation of turbulent kinetic energy (ε) equation:

$$\frac{\partial}{\partial t}(\rho \varepsilon) + \frac{\partial}{\partial x_k}(\rho u_k \varepsilon) = \frac{\partial}{\partial x_k}\left(\left(\frac{\mu_l}{\mathrm{Pr}} + \frac{\mu_t}{\sigma_\varepsilon}\right)\frac{\partial \varepsilon}{\partial x_k}\right) + S_\varepsilon$$

Species mass fraction (Z):

$$\frac{\partial}{\partial t}(\rho Z) + \frac{\partial}{\partial x_k}(\rho u_k Z) = \frac{\partial}{\partial x_k}\left(\left(\frac{\mu_l}{\mathrm{Pr}} + \frac{\mu_t}{\sigma_c}\right)\frac{\partial Z}{\partial x_k}\right)$$

where ρ, u_i, p, H are the density, velocity components, pressure and total enthalpy respectively and $\mu = \mu_l + \mu_t$ is the total viscosity; μ_l, μ_t being the laminar and turbulent viscosity and Pr is the Prandtl number. The source terms S_k and S_ε of the K and ε equation are defined as

$$S_K = \tau_{ik}\frac{\partial u_i}{\partial x_k} - \rho\varepsilon \quad \text{and} \quad S_\varepsilon = C_{\varepsilon 1}\tau_{ik}\frac{\partial u_i}{\partial x_k} - C_{\varepsilon 2}\frac{\rho\varepsilon^2}{K}$$

where turbulent shear stress is defined as

$$\tau_{ik} = \mu_t\left(\frac{\partial u_i}{\partial x_k} + \frac{\partial u_k}{\partial x_i}\right)$$

Laminar viscosity (μ_l) is calculated from the Sutherland law as

$$\mu_l = \mu_{ref}\left(\frac{T}{T_{ref}}\right)^{3/2}\left(\frac{T_{ref} + S}{T + S}\right)$$

where T is the temperature and μ_{ref}, T_{ref} and S are known coefficients. The turbulent viscosity μ_t is calculated as

$$\mu_t = c_\mu \frac{\rho K^2}{\varepsilon}$$

The coefficients involved in the calculation of μ_t are taken as

$$c_\mu = 0.09, \qquad C_{\varepsilon 1} = 1.44, \qquad C_{\varepsilon 2} = 1.92$$

$$\sigma_K = 1.0, \qquad \sigma_\varepsilon = 1.3, \qquad \sigma_c = 0.9$$

The heat flux q_k is calculated as $q_k = -\lambda \frac{\partial T}{\partial x_k}$, λ is the thermal conductivity.

3.2. Thermodynamics model

A thermally perfect gas is assumed in the present study and, consequently, the specific heats for all species are function of temperature only. The specific heats are calculated using a fourth-order polynomial at the interval of fluid temperature 300–5000 K. In each interval, the same form for the polynomials is used but different coefficients can be used.

$$\frac{C_{p_i}}{R} = A_i + B_i T + C_i T^2 + D_i T^3 + E_i T^4$$

where A_i, B_i, C_i, D_i and E_i are curvefit constants [15] and T is the fluid static temperature. C_{p_i} is linearly extrapolated when the fluid temperature $T > 300$ K or $T < 5000$ K. Then, the static enthalpy h is calculated as $h = \sum_{i=1}^{n} \alpha_i h_i(T)$ and the static enthalpy of each species $h_i(T)$ is

$$h_i(T) = \Delta h^o_{fi} + \int_{T^0}^{T} C_{p_i}(T)\, dT$$

where Δh^o_{fi} is the standard heat of formation of species i, defined as the heat evolved when one mole of substance is formed from its elements in their respective standard states at 298.15 K and 1.0 atmosphere. The fluid temperature is calculated based on the solution of the fluid enthalpy using a Newton's iteration method for finding the roots of the polynomials. An equation of state of the following form for a multi-component is used to calculate fluid density $\rho = P/(RT/M_w)$, where the mixture molecular weight is obtained by the following equation, $M_w = (\sum_{i=1}^{n}(\alpha_i/M_w))^{-1}$ and R is the universal gas constant.

The Gibbs free energy is required to determine the equilibrium constants for the combined eddy dissipation and finite rate chemistry models. It is obtained for a constant pressure process by

$$\frac{g_i}{R} = A_i(T - \ln T) - \frac{B_i}{2}T^2 - \frac{C_i}{6}T^3 - \frac{D_i}{12}T^4 - \frac{E_i}{20}T^5 + F_i - G_i T$$

where G_i is an additional curvefit constant.

3.3. Combustion modeling

The combustion model used for the simulation is a combination of Eddy Dissipation (ED) model and Finite Rate Chemistry (FRC) model to calculate effective reaction rate. The reaction rate is calculated by using single step chemistry, and for the following reversible reaction has been chosen.

$$2H_2 + O_2 \Leftrightarrow 2H_2O$$

The combined model is computed to be the minimum of the ED rate and the FRC rate. In the ED model, the chemical reaction is fast relative to the transport processes in the flow. When reactants mix at the molecular level, they instantaneously form products. The model assumes that the reaction rate may be related directly to the time required to mix reactants at the molecular level. In turbulent flows, this mixing time is dominated by the eddy properties and, therefore, the rate is proportional to a mixing time defined by the turbulent kinetic energy (K) and dissipation (ε), i.e., reaction rate $\alpha\varepsilon/K$. The mixing rate determined from the ED model is given as

$$R_{H_2,edm} = A_{ed}\overline{\rho}\frac{\varepsilon}{k}\min\left\{Y_f, \frac{Y_o}{\nu_{H_2}}, B_{ed}\frac{Y_p}{1+\nu_{H_2}}\right\}$$

where Y_f, Y_o and Y_p are the mass fraction of fuel, oxidant and products respectively, A_{ed} and B_{ed} are model constants, ν_{H_2} is stoichiometric coefficients of H_2 reaction. In FRC model the kinetic rate of change of any species (H_2, O_2 and H_2O) in a reaction is generally described by Arrhenius expression involving an exponential dependence on temperature and power law dependence on the concentrations of the reacting chemical species. The rate of reaction of $R_{H_2,frc}$ (in kg mol/m^3 s) is given by the expression [3,4]

$$R_{H_2,frc} = -2\left\{1.102 \times 10^{19} * \exp(-8052/T)c^2_{H_2}c_{O_2} - \kappa_b c^2_{H_2O}\right\}$$

where c is the molar concentration (in g mol/cm^3) and κ_b, the rate constant of backward reaction, is obtained from the forward rate constant and equilibrium constant ($\kappa_b = \kappa_f/\kappa_e$), where κ_f and κ_e are forward rate constant and the equilibrium coefficient respectively, it can be written as $\kappa_e = (RT)^{-2}\exp(-2g_i/RT)$.

The rate of reaction is then determined from the minimum of the mixing and kinetic net rate and is expressed as

$$R_{H_2} = \min(R_{H_2,edm}, R_{H_2,frc})$$

The finite rate turbulence–chemistry interaction model through source term is difficult and need extra models. Such interactions are not considered in the present study.

3.4. Discretization of governing equations

The CFX-11 solver utilizes a finite volume approach, in which the conservation equations in differential form are integrated over a control volume described around a node, to obtain an integral equation. The pressure integral terms in the momentum integral equation and the spatial derivative terms in the integral equations are evaluated using finite element approach. An element is described with eight neighboring nodes. The advective term is evaluated using upwind differencing with physical advection correction. The set of discretized equations form a set of algebraic equations: $A\vec{x} = b$, where $\vec{x}$ is the solution vector. The solver uses an iterative procedure to update an approximated x_n (solution of x at nth time level) by solving for an approximate correction x' from the equation $A\vec{x'} = \vec{R}$, where $\vec{R} = \vec{b} - A\vec{x}_n$ is the residual at nth time level. The equation $A\vec{x'} = \vec{R}$ is solved approximately using an approach called Incomplete Lower Upper factorization method. An algebraic multigrid method is implemented to reduce low frequency errors in the solution of the algebraic equations. Maximum residual $(= \varphi_j^{n+1} - f(\varphi_j^{n+1}, \varphi_j^n)) < 10^{-4}$ is taken as convergence criteria.

4. Results and discussion

As mentioned earlier, the injection holes are equal in size and placed in equi-distance along the width, the combustor geometry is symmetry around the holes and adjacent region. However, this geometrical symmetry is not present the wall-adjacent holes. One injection hole along with both side adjacent regions (up to middle of the two adjacent injection holes) has been considered for the computational domain. The supersonic inflow condition corresponding to Mach 2.0 is imposed at the inflow boundary. Both

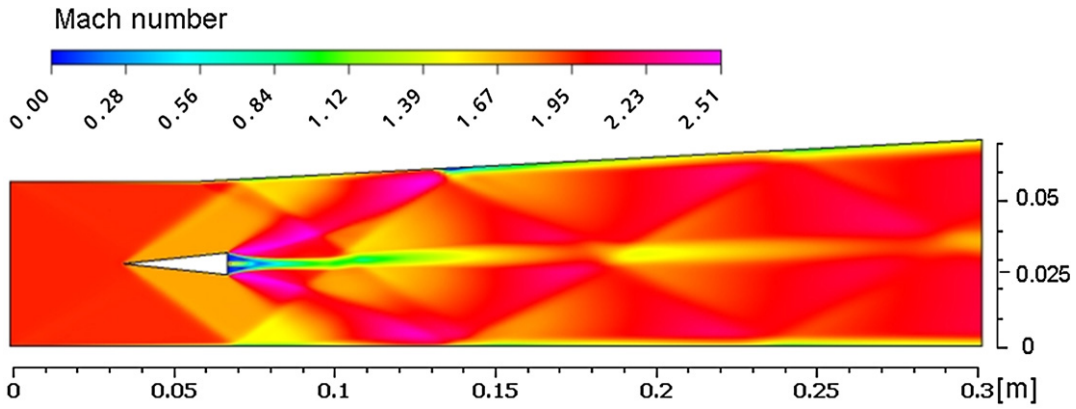

Fig. 3. Mach number distribution on mid-plane of combustor width ($Z = 0.0$).

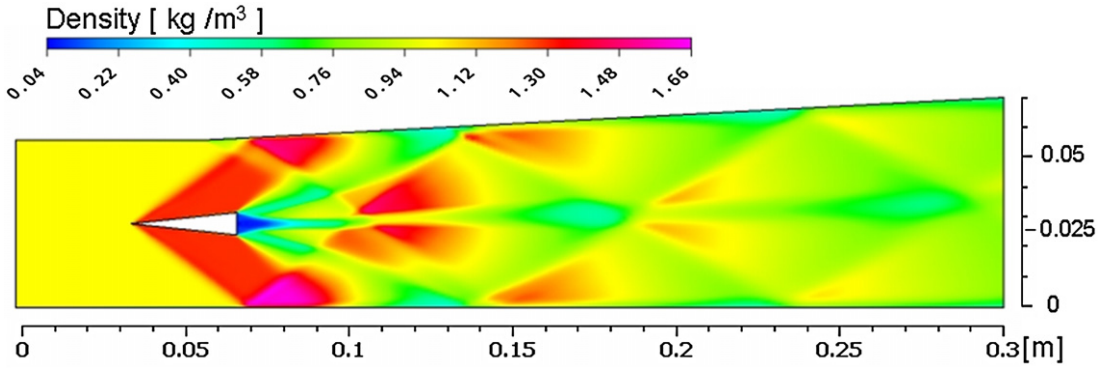

Fig. 4. Density distribution on mid-plane of combustor width ($Z = 0.0$).

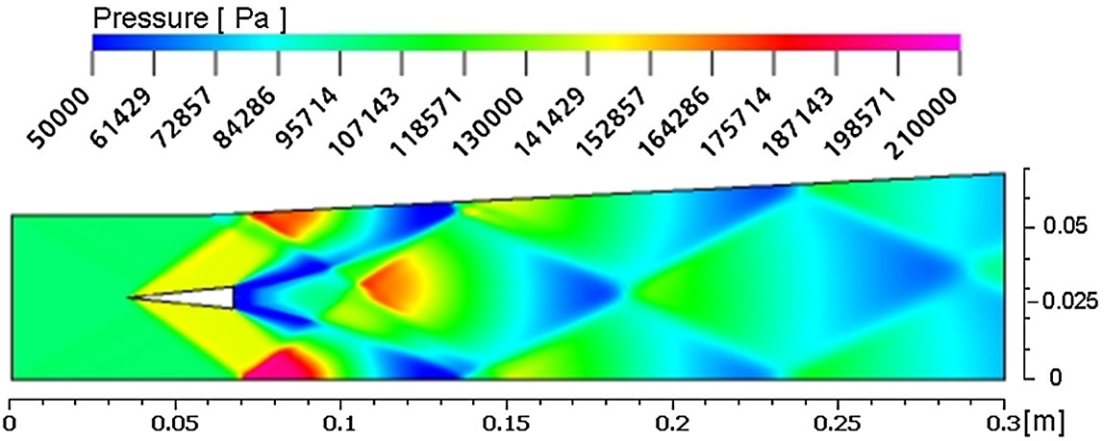

Fig. 5. Static pressure distribution on mid-plane of combustor width ($Z = 0.0$).

non-reacting (with mass addition) and reacting simulations are carried out.

4.1. Non-reacting flow simulation

In the simulation, sonic hydrogen gas is injected parallel to air flow ($M_a = 2.0$) from the base of the strut. Hydrogen is considered as inert gas without any combustion. The Mach number distribution at the mid-plane of the combustor width ($Z = 0$) is shown in Fig. 3.

The complex shock structures from the leading edge and the expansion waves from the base of the struts and their reflections from the walls are crisply captured in the simulation. Thin boundary layers at both upper and lower walls are seen in the figure. The complex flow pattern in the wake region of the strut is seen in the mid-plane pressure and density distribution presented in Figs. 4 and 5 respectively.

Experimental shadowgraph and numerical schlieren (density gradient) are compared in Fig. 6 to depict the position of the shocks and their interaction and the numerical simulation exhibits all detailed flow structures as seen in the experiment. The computed static pressure distributions at bottom wall are compared in Fig. 7(a). The oblique shockwave generated from the leading edge is hitting the lower wall at $X = 0.07$ m from the combustor entry. Both the magnitude and location of the pressure rise are correctly matched with the experimental result. Although, the location ($X \sim 0.136$ m) of the second reflection point is predicted correctly, the computation underpredicts the second shock strength.

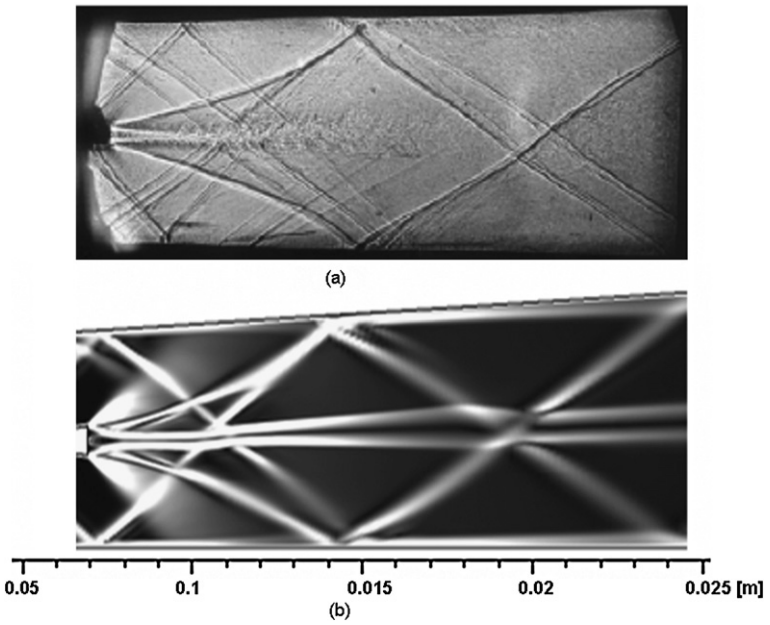

Fig. 6. Comparison of (a) experimental shadowgraph with (b) computational density gradient.

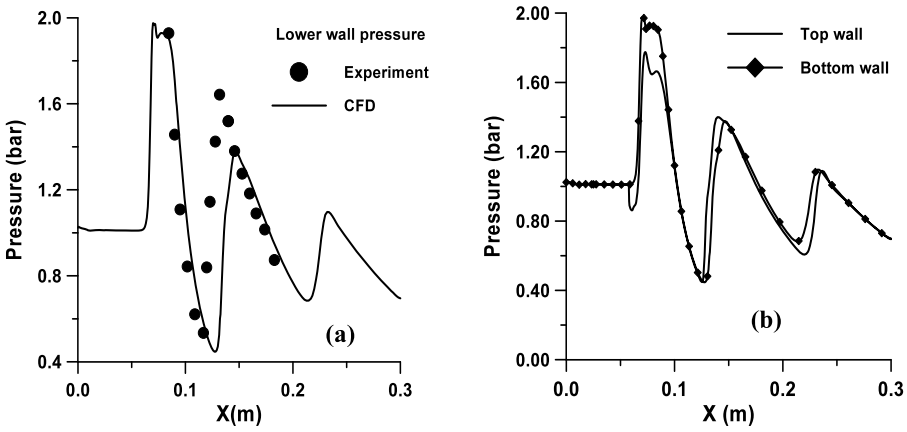

Fig. 7. Comparison of wall pressures: (a) experiment & CFD (lower wall), (b) upper & lower wall (CFD).

Computed static pressures at the upper and lower walls are compared in Fig. 7(b). Both the pressures are following the same trend except at the first reflection point where the lower wall exhibits about 11% higher pressure.

The comparison of static pressure at the center line of the combustor (line passing through the center of the H_2 injector, $Y = 0.025$ m) is shown in Fig. 8. Overall good match is observed between the experiment and present computation except at $X = 0.11$ m (0.043 m downstream of hydrogen injection plane) where experimental value is higher than the computed results. The profiles of the axial velocity (u velocity) component at four different stream-wise locations ($X = 0.078$, 0.125, 0.157 and 0.233 m) are compared with experiment results in Fig. 9. A very good match is observed between the computed and the experimental results. The magnitude of the velocity defect in the strut wake region is diminishing as we proceed downstream.

The performance of the combustor in non-reacting flow with mass addition is characterized by mixing efficiency which is defined as:

$$\eta_m = \frac{\int_A \alpha \rho_{gas} Y_{H_2} u \, dA}{\dot{m}_{H_2}}, \quad \text{with } \alpha = \begin{cases} 1, & \phi < 1 \\ 1/\phi, & \phi \geqslant 1 \end{cases}$$

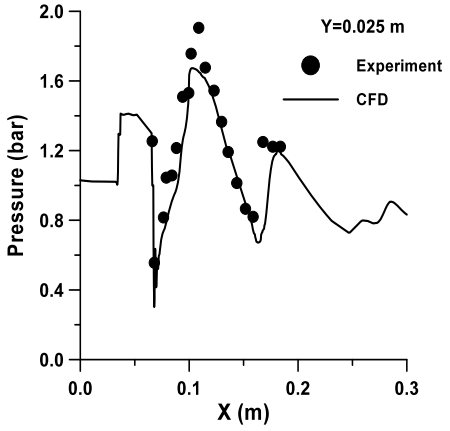

Fig. 8. Comparison of static pressure at middle of combustor height ($Y = 0.025$ m).

where ρ_{gas} is the gas density, Y_{H_2} is the mass fraction of hydrogen with $Y_{H_2} = \rho_{H_2}/\rho_{gas}$, ρ_{H_2} is the density of hydrogen, A is the cross-sectional area, and u is the axial velocity. ϕ is the local equivalence ratio which is defined as $\phi = (M_{O_2} Y_{H_2}/2M_{H_2} Y_{O_2})$ where

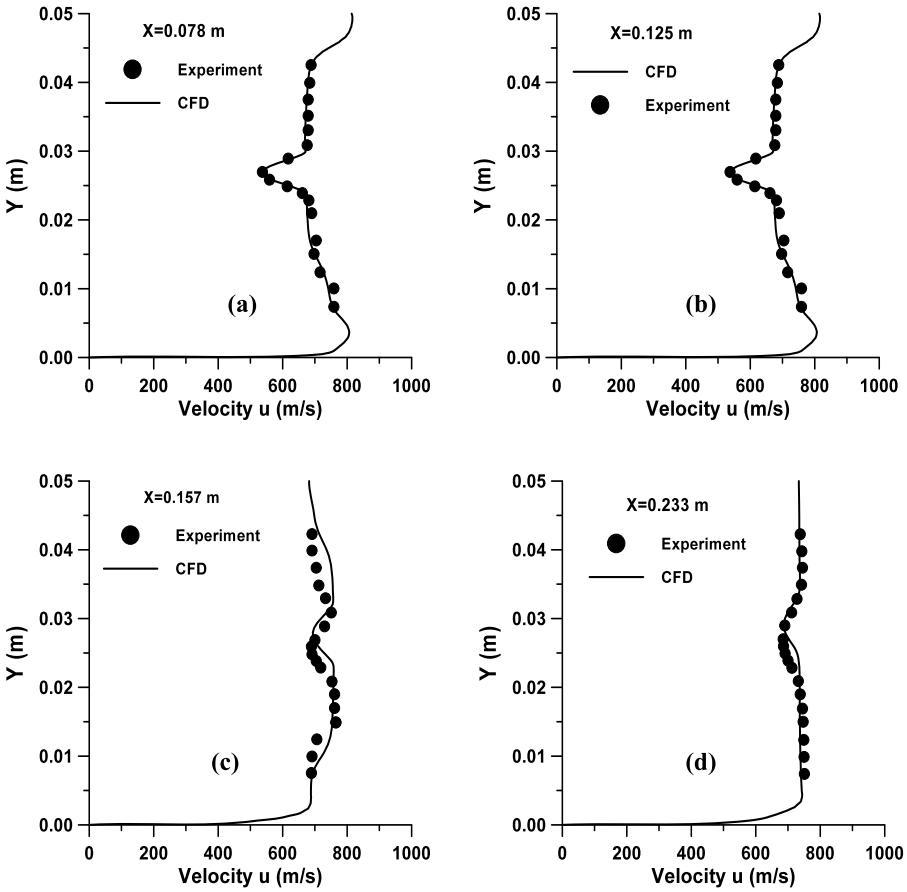

Fig. 9. Comparison of axial velocity (u) profile at various axial locations: (a) $X = 0.078$ m, (b) $X = 0.125$ m, (c) $X = 0.157$ m and (d) $X = 0.233$ m.

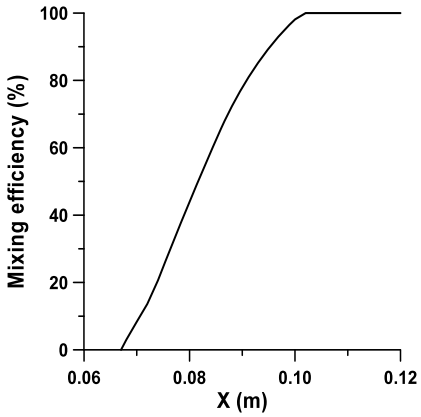

Fig. 10. Mixing efficiency for non-reacting flow.

M_{O_2} and M_{H_2} are the molecular weights of oxygen and hydrogen respectively, and Y_{O_2} is the mass fraction of oxygen. The distribution of the mixing efficiency along the length of the combustor is shown in Fig. 10.

4.2. Reacting flow simulation

Reacting flow simulation has been carried out with the reaction of hydrogen fuel in vitiated air. Based on mass flow of air and hydrogen, the stoichiometric ratio is calculated to $\phi = 0.0276$. Single step reaction considering H_2 and O_2 as reactant and H_2O as product is considered for the simulation. The density field at the mid-plane of the combustor width ($Z = 0$) is shown in Fig. 11.

Comparing the density field with the non-reacting case (Fig. 4), we can observe that the heat release due to reaction has reduced the density in the wake region of the strut. Also, the shock structures are weakened significantly in the downstream due to the combustion of hydrogen fuel.

The distribution of H_2O vapor mass fraction at the mid-plane of the combustor width ($Z = 0$) presented in Fig. 12 clearly depicts the reaction zone in the combustor. It is seen that combustion has occurred in a narrow zone from the base of the strut and the fuel has not spread enough in the lateral direction. Both the near wall zones remain unaffected even after the combustion is completed mainly because the injection is parallel and the low fuel mass flow rate ($\phi = 0.0276$).

The comparison of computed axial velocity (u velocity) distribution with experiment at $Y = 0.025$ m is presented in Fig. 13. The high speed hydrogen fuel sharply decelerated from 1200 m/s (injection velocity of hydrogen) to about 200 m/s within short distance of ~ 0.003 m. The axial velocity remains almost constant in the reaction intense zone (up to $X = 0.11$ m), afterwards, the velocity gradually increases in the divergent combustor. The trend of the present results matches well with the experiment, however, computed axial velocity is higher. Comparisons of axial velocities at different cross sections (at $x = 0.078$, 0.125, and 0.207 m) presented in Fig. 14 reveal that the computed velocity profile near wake region is matching well with the experimental values, while it overpredicts the velocity in the far wake region. A better grid density may be required to resolve the differences.

The computed temperature profiles at the same axial locations ($X = 0.078$, 0.125 and 0.233 m) are compared with the experimental result in Fig. 15. Clearly the reaction is confined at the

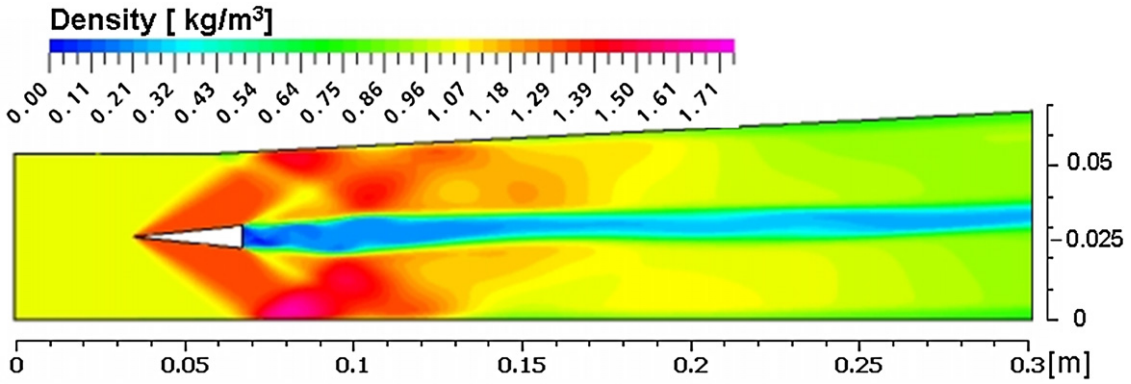

Fig. 11. Density contour distribution at mid-plane of combustor width ($Z = 0.0$).

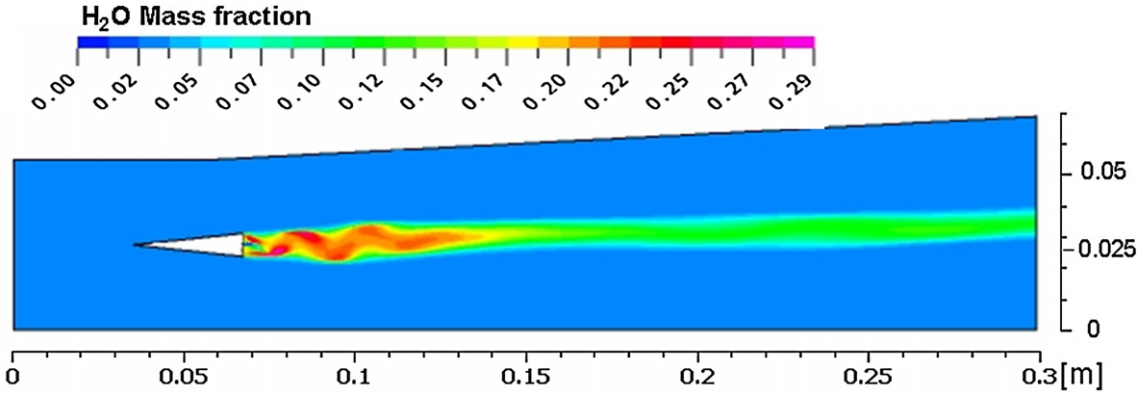

Fig. 12. H_2O mass fraction distribution at mid-plane of combustor width ($Z = 0.0$).

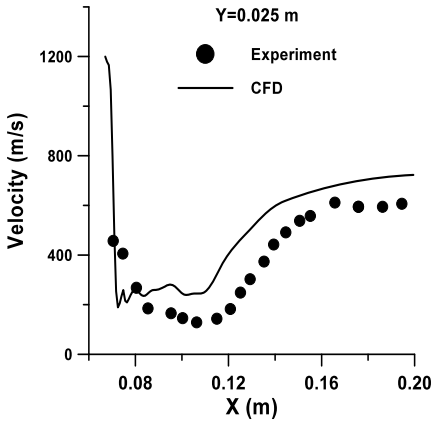

Fig. 13. Comparison of axial velocity at middle of the combustor height ($Y = 0.025$ m).

central zone of the combustor downstream of the strut. The extent of the combustion zones is about $10d$ (d is diameter of injection hole) in the middle along the height of the combustor. The zone of combustion slightly moves upwards (towards the top wall) in the downstream region. A good overall trend between the experiment and the computation is predicted. The computed value of temperature distribution in the reaction zone in the near wake region ($X = 0.078$ m) is higher compared to the experimental data. This is due to instantaneous heat release due to fast chemistry assumption. A detailed H_2–air chemical kinetics is necessary to predict the finer details of the flow field in the near wake region.

The distribution of combustion efficiency along the length of the combustor has been shown in Fig. 16. Combustion efficiency is defined by the following formula:

$$\eta_c = 1 - \frac{\int_A \rho_{gas} Y_{H_2} u \, dA}{\dot{m}_{H_{2,inj}}}$$

which describes how much of the injected fuel has been consumed since injection.

From the results it has been observed that the combustion has been completed within an axial distance of 0.063 m from the base of the strut (H_2 mass $\sim 0.02\%$ of total H_2).

4.3. The effect of periodic boundary condition on the flow field

New simulations were carried out by considering the full combustor. Taking advantage of the symmetry, only one half of the combustor is simulated along with seven and half injectors. A total $420 \times 65 \times 78$ grids consisting of 2.13 millions computational volumes are used in the simulation. All the wall boundary layers (top, bottom and side) were well resolved in the numerical simulation. Minimum y^+ at the wall is about 10. Since no information on the boundary layer at the combustor entry is available, additional simulation is carried out with initial boundary layer thickness of 5 mm and the results are compared with no initial boundary layer case. 1/7th power law is fitted for the velocity profile at the combustor entry. The computed water mass fraction distributions for these two cases are presented in Fig. 17.

Comparing the water mass fraction distribution with the periodic boundary case (Fig. 12) we could see although the periodic boundary case is showing reaction closer to the strut base, a boarder and intense reaction zone is visible in the downstream

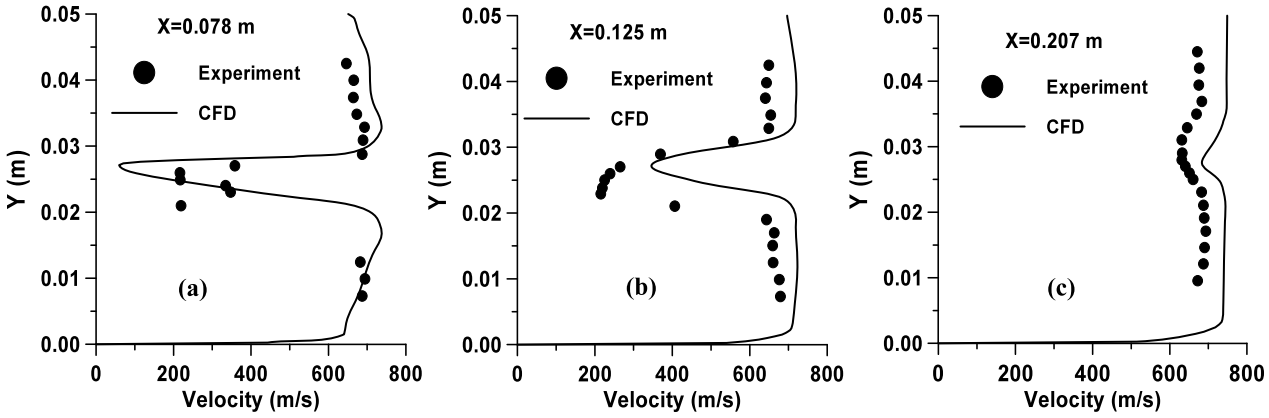

Fig. 14. Comparison of axial velocity profiles: (a) $X = 0.078$ m, (b) $X = 0.125$ m, (c) $X = 0.207$ m.

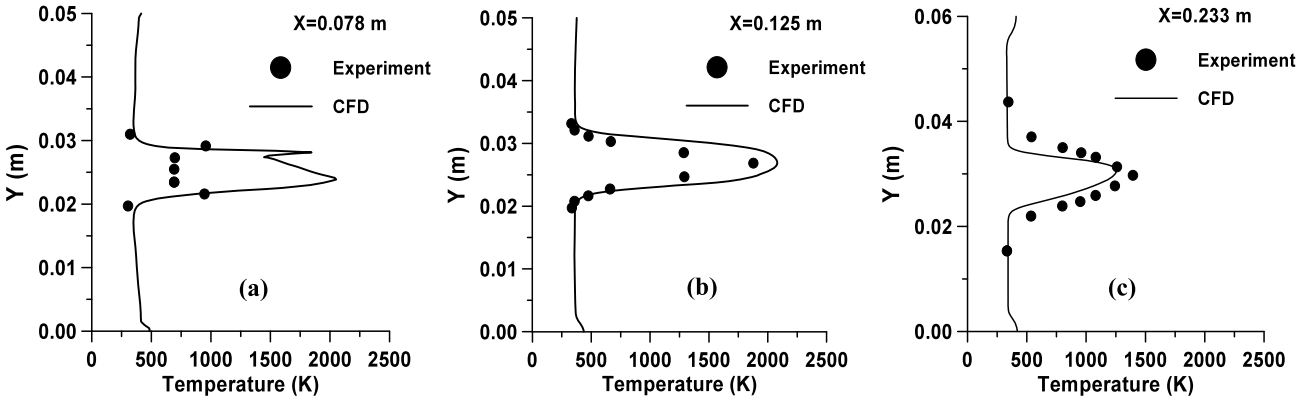

Fig. 15. Comparison of static temperature profiles: (a) $X = 0.078$ m, (b) $X = 0.125$ m, (c) $X = 0.207$ m.

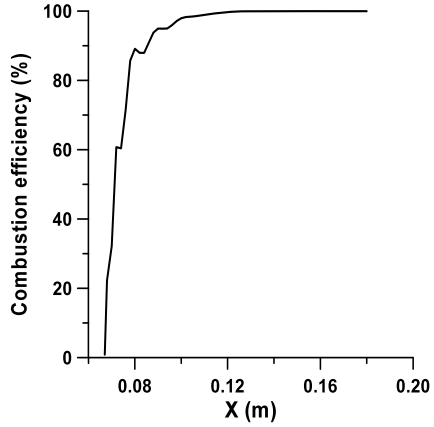

Fig. 16. Combustion efficiency for reacting flow.

regions for the full combustor simulation. It is observed that higher boundary layer thickness at the combustor entry resulted in shorter reaction zone in the near field of the strut. The computed centerline velocity distributions for the reacting case for all the three cases are compared with experimental data in Fig. 18. With the full combustor simulation, velocity has reduced significantly in the reaction zone indicating more intense reaction which collaborates well with the water mass fraction distribution. For 5 mm initial boundary layer case, there is marginal difference in the velocity distribution in the zone $0.08 \text{ m} < X < 1.1$ m.

The computed temperature profiles for different axial locations (0.078 m, 0.125 m and 0.233 m) are compared with the experimental values in Fig. 19 which reveal that the profiles from full combustor simulation are showing much better comparison (both in magnitude and structure) with the experimental values compared to the periodic boundary case. At the near strut location ($X = 0.078$ m), full combustor simulation is capturing the peaks and valleys of temperature profiles very well whereas the periodic boundary case is showing much higher temperature in the core of the wake region. This is due to the early onset of reaction in the periodic boundary condition case as discussed earlier. At the furthest location ($X = 0.233$ m) the maximum deviation of temperature is of the order of 12%. It may be recalled that the present simulation is using infinitely fast rate kinetics which is likely to yield higher computed temperature.

5. Concluding remarks

Mixing and combustion of hydrogen fuel injected parallely from the struts into Mach 2 vitiated air stream in a generic scramjet combustor are explored numerically. Both non-reacting and reacting flows are simulated. The generic scramjet combustor with hydrogen fuel injected from the base of the strut investigated at DLR in Germany is taken as the test case for validation. 3D Reynolds averaged Navier–Stokes equations are solved along with K–ε turbulence model using a commercial CFD software. Combustion of hydrogen gas with air was modeled with combined Eddy Dissipation Model (EDM)/single step Finite Rate Chemistry (FRC). The simulations crisply capture the complex flow structure including the leading shock waves generated from the leading edge of the fuel injection strut, expansion fan from the base of the strut and the interaction of shock reflections from the walls in non-reacting flow. The results of wall pressures and axial velocities match well

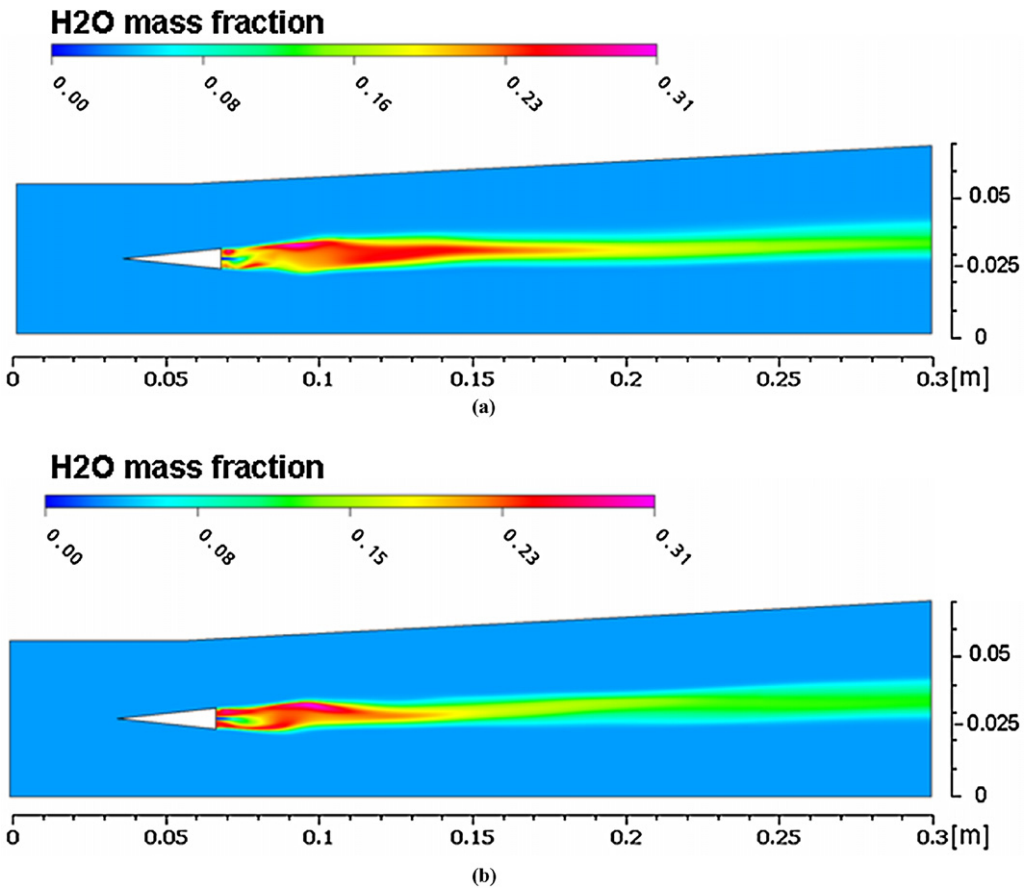

Fig. 17. H_2O mass fraction distribution at mid-plane of combustor width ($Z = 0.0$): (a) 0 BL, (b) 5 mm BL.

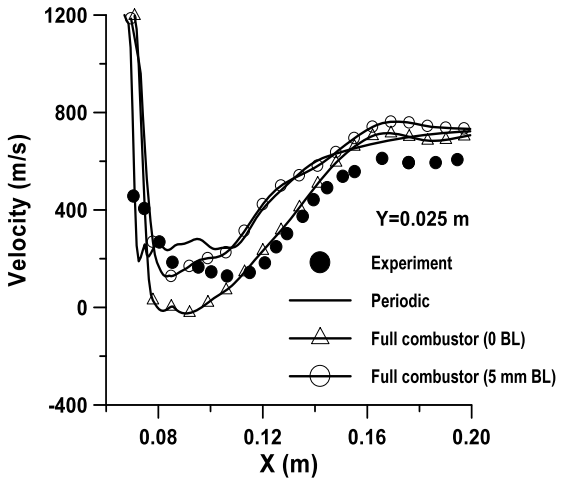

Fig. 18. Comparison of centerline velocity.

with the experiment. In the reacting flow, the presence of reaction has weakened the shock structure. Reaction of hydrogen fuel has occurred within a narrow zone ($\sim 10d$ diameter) at the middle of the combustor. The computed velocity profile matches well in the near wake region, while the computation overpredicts the velocity in the far wake region. The effect of the periodic boundary condition on the scramjet combustor is studied by carrying out the simulation with full geometry and comparing the results with periodic boundary case. It has been observed that the periodic boundary condition predicts early onset of reaction but the reaction zone is much boarder and intense for the full combustor simulation. Full combustor simulations predict the temperature profile accurately with maximum deviation with experimental value is of the order of 12%. A detailed H_2–air chemical kinetics is required for resolving the difference. Higher boundary layer thickness at the combustor entry resulted in shorter reaction zone in the near field of the strut. The initial boundary layer does not have significant impact in the flow development in the scramjet combustor. It has been observed that while simple engineering turbulence and combustion model is adequate for predicting the overall mixing and combustion process of hydrogen combustion but a detailed description of turbulence and chemistry is required for predicting the finer details of the flow field.

References

[1] ANSYS CFX, Release 11.0: Installation and Overview, January 2007.
[2] M. Berglund, C. Fureby, LES of supersonic combustion in a scramjet engine model, Proceedings of the Combustion Institute 31 (2007) 2497–2504.
[3] Debasis Chakraborty, P.J. Paul, H.S. Mukunda, Evaluation of combustion models for high speed H_2/air confined mixing layer using DNS data, Combustion and Flame 121 (2000) 195–209.
[4] J.P. Drummond, M.H. Carpenter, D.W. Riggins, in: S.N.B. Murthy, E.T. Curran (Eds.), High Speed Propulsion System, in: Progress in Aeronautics and Astronautics, vol. 137, 1991.
[5] F. Genin, B. Chernyavsky, S. Menon, Large eddy simulation of scramjet combustion using a subgrid mixing/combustion model, AIAA Paper 2003-7035, 2003.
[6] P. Gerlinger, P. Kasal, P. Stoll, D. Bruggemann, Experimental and theoretical investigation on 2D and 3D parallel hydrogen/air mixing in a supersonic flow, ISABE Paper 2001-1019, 2001.
[7] D.D. Glawe, M. Saminy, A.S. Nejad, T.H. Cheng, Effects of nozzle geometry on parallel injection from base of an extended strut into a supersonic flow, AIAA Paper 95-0522, 1995.
[8] W. Heiser, D. Pratt, Hypersonic Airbreathing Propulsion, Education Series, AIAA, 1994.
[9] A. Javed, D. Chakraborty, Numerical simulation of supersonic combustion of pylon injected hydrogen fuel in scramjet combustor, Journal of the Institution of Engineers (India) 87 (May 2006) 1–6.

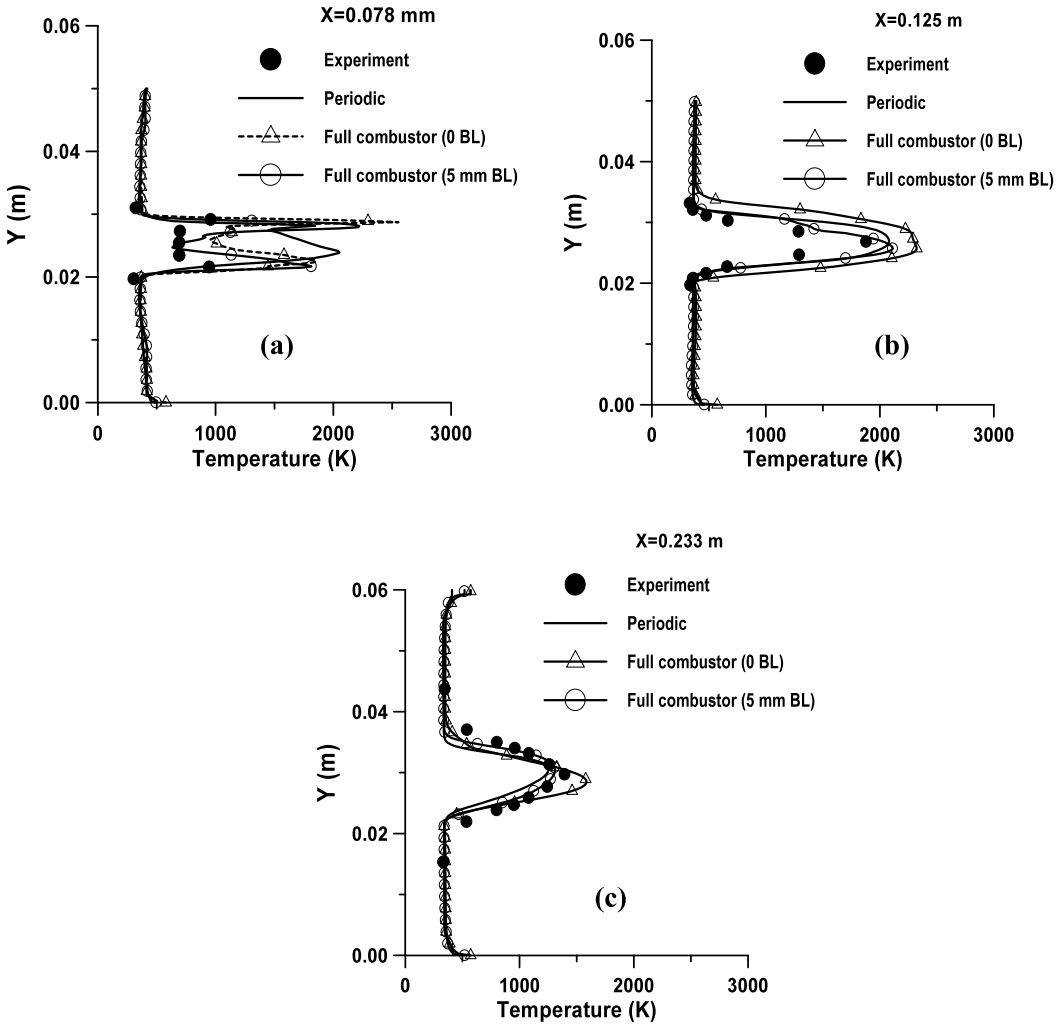

Fig. 19. Comparison of static temperature profiles at different axial locations: (a) $X = 0.078$ m, (b) $X = 0.125$ m, (c) $X = 0.233$ m.

[10] P. Manna, D. Chakraborty, Numerical investigation of transverse sonic injection in a nonreacting supersonic combustor, Proc. IMechE Part G: J. Aerospace Engineering 219 (2005) 205–215.
[11] P. Manna, D. Chakraborty, Numerical simulation of transverse H_2 combustion in supersonic airstream in a constant area duct, Journal of the Institution of Engineers (India) 86 (November 2005) 47–53.
[12] G. Masuya, T. Komuro, A. Murakami, N. Shinozaki, A. Nakamura, M. Murayama, K. Ohwaki, Ignition and combustion performance of scramjet combustor with fuel injection struts, Journal of Propulsion and Power 11 (2) (1995) 301–307.
[13] T. Mitani, N. Chinzei, T. Kanda, Reaction and mixing-controlled combustion in scramjet engines, Journal of Propulsion and Power 17 (2) (2001) 308–313.
[14] T. Mitani, T. Kanda, T. Hiraiwa, Y. Igarashi, T. Nakahashi, Drags in scramjet engine testing – Experimental and computational fluid dynamics studies, Journal of Propulsion and Power 15 (4) (1999) 578–583.
[15] Michael Oevermann, Numerical investigation of turbulent hydrogen combustion in a scramjet using flamelet modeling, Aerospace Science Technology 4 (2000) 463–480.
[16] S. Saha, D. Chakraborty, Reacting flow computation of staged supersonic combustor with strut injection, AIAA Paper 2006-3895, 2006.
[17] J.M. Seiner, S.M. Dash, D.C. Kenzakowski, Historical survey on enhanced mixing in scramjet engines, Journal of Propulsion and Power 17 (6) (2001) 1273–1286.
[18] S. Tomioka, K. Kobayashi, K. Kudo, A. Murakami, T. Mitani, Effects of injection configuration on performance of a stage supersonic combustor, Journal of Propulsion and Power 19 (5) (2003) 876–884.
[19] S. Tomioka, A. Murakami, K. Kudo, T. Mitani, Combustion tests of a staged supersonic combustor with a strut, Journal of Propulsion and Power 17 (2) (2001) 293–300.
[20] W. Waidmann, F. Alff, M. Bohm, U. Brummund, W. Clauss, M. Oschwald, Experimental investigation of hydrogen combustion process in a Supersonic Combustion Ramjet (SCRAMJET), in: DGLR Jahrbuch, 1994, pp. 629–638.
[21] W. Waidmann, F. Alff, M. Bohm, U. Brummund, W. Clauss, M. Oschwald, Supersonic combustion of hydrogen/air in a scramjet combustion chamber, Space Technology 15 (6) (1995) 421–429.
[22] W. Waidmann, U. Brummund, J. Nuding, Experiments investigation of Supersonic Ramjet Combustion (Scramjet), in: 8th International Symposium on Transport Phenomena in Combustion, San Francisco, USA, 1995.
[23] Ulrich Wepler, W. Kaschel, Numerical investigation of turbulent reacting flows in a scramjet combustor model, AIAA Paper 2002-3572, 2002.